

# Hierarchical Random Walker Segmentation for Large Volumetric Biomedical Data

Dominik Drees, Xiaoyi Jiang

**Abstract**—The random walker method for image segmentation is a popular tool for semi-automatic image segmentation, especially in the biomedical field. However, its linear asymptotic run time and memory requirements make application to 3D datasets of increasing sizes impractical. We propose a hierarchical framework that, to the best of our knowledge, is the first attempt to overcome these restrictions for the random walker algorithm and achieves sublinear run time and constant memory complexity. The method is evaluated on synthetic data and real data from current biomedical research, where high segmentation quality is quantitatively confirmed and visually observed, respectively. The incremental (i.e., interaction update) run time is demonstrated to be in seconds on a standard PC even for volumes of hundreds of Gigabytes in size. An implementation of the presented method is publicly available in version 5.2 of the widely used volume rendering and processing software Voreen<sup>1</sup>.

## I. INTRODUCTION

While the study of structures in 3D datasets is important in many contexts, especially in the biomedical field [4], [6], [21], visual inspection based analysis is error-prone [23]. For quantifiable results or novel insights into properties of the data invisible to the human observer, automatic techniques are required. For many analysis techniques (from simple volume/area comparisons to complex structure analysis [14]) binary segmentation is an important intermediate step. At the same time, improvements in imaging technologies (for example in light sheet microscopy) are providing images of increasing resolution and size (with hundreds of Gigabytes or even Terabytes for a single dataset). While this opens the door for biomedical research [26], [44], it also poses problems for image analysis algorithms that need to be solved to further advance biomedical and other research with new technology providing quantifiable results.

The random walker method for image segmentation [18], [37] is a popular technique for interactively creating arbitrary segmentations of 3D (or 2D) datasets. From user-defined initial seeds for semantically different regions of the image, the complete image is labeled based on local connectivity and voxel-wise similarity. A problem for the application of this technique on larger datasets is its lacking scalability: For a dataset with  $n$  voxels, it requires  $\Theta(n)$  memory (with a high constant factor) and  $\Omega(n)$  computation time even for a very local update of the set of seeds. In practice, even for datasets smaller than 100 MB, minutes of computation time and large portions of the available graphics or main memory of

a standard PC are required, a problem that is not fundamentally solved by earlier extensions to the method [37].

**Contributions:** We present a hierarchical, level-of-detail (LOD) pyramid-based framework that, to the best of our knowledge for the first time, allows random walker image segmentation to be applied to out-of-core (i.e., larger than main memory) datasets. The core idea of hierarchical refinement of an initial coarse application of the basic method in constant sized bricks achieves constant memory requirements while further optimizations such as pruning result in an observed sublinear run time. Using our technique, incremental updates can often be computed in seconds even for 100 GB and larger volumes. While this paper focuses on binary image segmentation and the 3D case, a generalization to multi-class labeling and to 2D data is conceivable.

The remainder of the paper is organized as follows. After presenting related work and two fundamental concepts, the proposed framework will be described in detail. Subsequently, an evaluation on synthetic data and real data from current biomedical research is presented and discussed, followed by the conclusion.

## II. RELATED WORK

The seminal work of Grady [18] is the basis of a large number of publications with applications in biomedicine (fluorescent cell tracking [35], pap smear cells [10], tumor [40], [41], placenta [30], airway segmentation [34], [42], multimodal problems [3], [2]) and geophysical research [17]). It is also used in other algorithms (image superpixel segmentation [33] and deep learning techniques [28]).

Research to extend the basic idea is still ongoing, for example on automatic seed generation [1]. Yang et al. augmented the method for interactive boundary definition [43]. The automatic choice of edge weighting functions has been tackled using statistical models [5] and an end-to-end learning [9]. Prassni et al. [32] proposed uncertainty visualization guiding label placement in interactive 3D volume segmentation. However, resource requirements of the random walker method hinder application in some cases. Xiao and Hu [39] apply Grady's method in a two-step ("hierarchical") procedure to first identify an abnormal region and then a tumor within. They note that during the evaluation "12 groups failed due to high space complexity of RW".

Ge et al. [16] propose a hierarchical strategy for the related graph-cut method [7]. The authors suggest creating an initial segmentation on the coarsest level of a LOD-pyramid and using finer levels for refinement of segmentation boundaries.

D. Drees and X. Jiang are with University of Münster, Germany.

<sup>1</sup><https://www.uni-muenster.de/Voreen/>

Their method, however, neither reduces the memory requirements, nor results in sublinear run time, as the propagation of intermediate segmentation results to the next layer still operates on the whole image.

Fabijanska and Goclawski [15] apply the random walker method on superpixels. While reducing the size of the linear equation system by roughly 90%, the pre-processing step still requires random access to the full image and introduces two parameters, changes to which require a complete recomputation, hindering interactive use on large datasets.

To the best of our knowledge there is no prior work on frameworks that allow the random walker method to be applied to images that exceed the main or graphics memory.

Finally, artificial neural network approaches have become increasingly popular [24], [29] which, depending on the problem, network design and receptive field, may also be suitable for large volume segmentation. However, these approaches require reliable ground truth data for training or manual refinement of results, for which semi-automatic tools like our framework can be very time- and cost-saving.

### III. FUNDAMENTAL CONCEPTS

This section introduces two known, but vital components of the proposed framework: The octree data structure and the original random walker method.

#### A. Octree Data Structure

The problem of high performance rendering of large volumetric datasets is, at least partially, solved in visualization, often using an octree data structure (originally introduced by LaMar [27] and Weiler [38] and improved in recent years [8], [11], [36]). Volumes are stored on disk as a brick-based LOD-pyramid from which parts can efficiently be loaded into memory for ray casting.

Similarly, the base structure for the LOD-pyramid in this paper is an octree with nodes  $n \in N = N^8 \cup \{\epsilon\}$ . A node is either an octuple of child nodes ( $n = (c_0, \dots, c_7)$ ) or empty ( $n = \epsilon$ ). Voxels at any level of the pyramid are stored in *bricks* of  $s^3$  voxels ( $b \in \mathbb{R}^{s^3} = B$ ) with side length  $s$ . Each node has an associated brick (via  $\text{br}: N \rightarrow B$ ).  $\mathcal{P}(n)$  denotes the parent node of  $n$ :

$$\mathcal{P}(n) = \begin{cases} (c_0, \dots, c_7) & \exists i (0 \leq i \leq 7) : c_i = n \\ \epsilon & \text{else} \end{cases}$$

When converting a voxel-grid volume of dimensions  $d_x \times d_y \times d_z$  into an octree representation, voxels are chunked into  $\frac{d_x}{s} \times \frac{d_y}{s} \times \frac{d_z}{s}$  bricks, each forming a leaf in the octree. The tree is then constructed bottom-up by bundling  $2^3$  neighboring nodes of one level as children of a new parent node in the next, coarser level until only a single root node remains. The parent node's associated brick is generated by applying a  $2^3$  mean filter and downsampling the combined bricks of its children. Here we assume  $d_x = d_y = d_z = 2^i \cdot s$ , but other volume dimensions can be handled by dynamic transformation and handling of the volume border in the brick-local space. This data structure is illustrated in Figure 1 and described in more detail by Brix et al. [8].

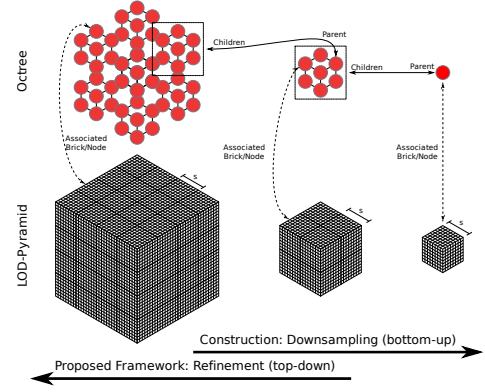


Fig. 1. LOD-Pyramid with Octree used for hierarchical processing. The full resolution dataset (bottom left) is divided into bricks of  $s^3$  voxels, each brick with an associated node.  $2^3$  nodes with neighboring bricks share a parent node. The parent node's brick is computed by downsampling its children's bricks. The root node's brick is a low resolution version of the input dataset. After the bottom-up construction of the octree, our method uses it in a top-down process.

#### B. Random Walker Volume Segmentation

The random walker image segmentation method [18] can be used to interactively generate arbitrary foreground/background segmentations in 3D (or 2D) images. The volume (or brick) is viewed as a 3D grid of vertices with edges between 6-neighbors. Vertices  $p \in [0, s]^3$  have associated weights defined by the intensity  $x(p) = b[p]$ , where brackets  $b[p]$  denote sampling the intensity from a brick or volume  $b$  at position  $p$ . Edge weights  $w_{p,q}$  are based on the similarity of the connected voxel vertices. Grady suggests  $w_{p,q} = \exp(-\beta(b[p] - b[q])^2)$  with  $\beta$  as a free parameter. When interpreting the image graph as an electrical circuit, edges are resistors with weights defining the conductance between vertices. Labeled vertices  $p_m \in V_m$  are voltage sources with a constant voltage of  $x(p) \in [0, 1]$ , which is set to 0 for background labels and 1 for foreground labels. The weight of an unlabeled vertex  $p_u \in V_u$ ,  $x(p_u)$ , is the resulting voltage and foreground probability. It can be computed by solving the discrete Dirichlet problem, i.e., by minimizing the Dirichlet integral  $D(x) = \frac{1}{2}x^T \mathcal{L}x = \frac{1}{2} \sum_{\|p-q\|=1} w_{p,q}(x(p) - x(q))^2$  with the boundary condition of predetermined  $x(p_m)$  and the Laplacian matrix  $\mathcal{L}$  of the image graph. A global minimum can be found by partitioning and reordering  $x$  according to  $V_u$  and  $V_m$  into  $x_u$  and  $x_m$  and solving  $\frac{dD(x_u)}{dx_u} = 0$ . While the minimization can be done analytically, it is often faster to use iterative approaches that additionally exploit the sparsity of  $\mathcal{L}$  [20]. The experiments in this paper use the conjugate gradient method for this purpose.

### IV. HIERARCHICAL FRAMEWORK: METHODS

This section first describes the core concept of our framework that has constant memory requirements, as well as two important extensions of the core idea. Then, a number of further considerations that greatly improve the run time as well as a partial update scheme for interactive segmentation are introduced.

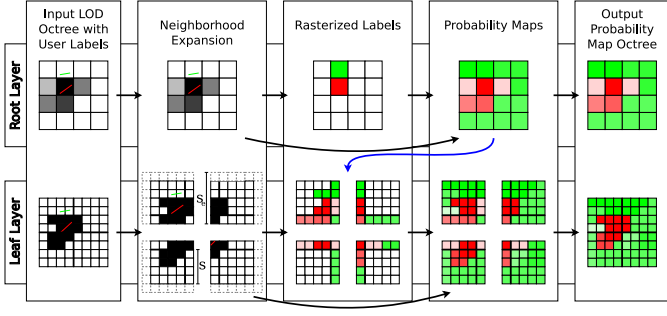


Fig. 2. Exemplary (2D) illustration of the proposed method: The input volume octree is processed top-down, rasterizing user labels for each brick and introducing global context into the local computation by initializing border seeds from solutions of a coarser level (blue arrow). These labels and the input volume brick are used as input for the random walker method which creates the output probability map for the current brick. In a more complex case, intermediate layers would be included in the top-down process, using the probability map of the previous layer and providing global context for the next layer via its probability map.

### A. Core Concept

The proposed method processes an input octree top-down and at the same time creates the output octree. In each layer, the random walker method for (3D) image segmentation [18] (or a suitable extension [37]) is used to process a brick of the input layer, thus creating a foreground probability map, one brick at a time. Labels are given as structures such as points or curves. Here, we define individual labels  $p \in P = \mathbb{R}^3 \times [0, 1]$  as 3D points with an associated seed value and label sets  $l \in L = 2^P$  as groups of labels.

For processing individual bricks, user-defined labels are transformed from volume space into local brick space using a transformation function  $\mathcal{T}_n: L \rightarrow L$  (comprising translation and scaling) defined for each node  $n$ . After the transformation, labels are rasterized to obtain brick-level seeds to be used in the random walker algorithm.

Let  $\text{rw}: B \times L \times \mathbb{R} \rightarrow B$  be the application of the random walker algorithm to a given input brick using a set of labels (in brick-local coordinates) and parameter  $\beta$ . Then, in the first, topmost layer of the LOD-pyramid, i.e., for the root node, the proposed procedure ( $\mathcal{H}: N \times L \times \mathbb{R} \rightarrow N$ ) does not differ much from the basic random walker approach:

$$\text{br}(\mathcal{H}(n, l, \beta)) = \text{rw}(\text{br}(n), \mathcal{T}_n(l), \beta) \quad (1)$$

The output is only defined by the input volume, user labels and  $\beta$ . For subsequent layers, however, the solution for the coarser layer serves as an approximation of the *true* probability map at the current level (if hypothetically computed on the full volume at the current LOD level) and is used to add additional *continuous labels* (with values in the range  $[0, 1]$ , but not necessarily either 0 or 1) at the border of the current brick, i.e., by upsampling from the coarser level probability map. This way, *global context* (either directly from the parent layer, or transitively via one of its parents) is introduced into the *local* foreground probability map. An example of how a labeled object influences the probabilities in a neighboring brick is illustrated in Figure 2.

The algorithm finishes after processing all leaf level bricks, where the resulting probability bricks define the foreground probability map of the voxel-grid volume that was used to create the input octree.

The hierarchical, local application of the basic method makes the presented approach applicable to arbitrarily large out-of-core datasets. Specifically, since individual bricks and resulting edge weight matrices are comparatively small (depending on  $s$ ), they can be stored in main or graphics memory. At the same time all computations are local to a single brick or its direct neighborhood, thus require few, linear disk accesses and can be GPU-accelerated. For experiments in this paper the brick size was set to  $s = 32$ . Larger brick sizes increase the memory requirement (as at least one brick at a time and the resulting linear equation system must be held in memory) and benefit less from pruning/incremental computation (see below). Much smaller bricks cause inaccurate results and disk reads to take a disproportionally large amount of time.

### B. Neighborhood Expansion

A remaining question is where the continuous seeds from coarser octree levels should be located. Placing them directly on the border of the current brick means that (since any non-root brick shares 3 of its 6 border faces with its parent, possibly even transitively) in the worst case global context is only established in the root node, so with low resolution. This would result in ragged edges in the resulting probability map. Hence, for the probability map computation the brick is expanded into its neighbors: The expanded brick side length  $s_e = \lfloor e \cdot s \rfloor$  is larger than the original brick by a factor  $e > 1$ . Let  $h \in \mathbb{R}^{s_e^3} = H$  be a brick neighborhood, and  $\text{nh}: N \rightarrow H$  and  $\text{ctr}: H \rightarrow B$  be retrieval and center brick extraction functions, respectively. Then continuous labels ( $\text{cl}: N \times L \rightarrow L$ ) are added at the border ( $\text{brd}: H \rightarrow L$ ) of the expanded brick, where the probability values are (up-) sampled ( $\text{smp}: N \times (\mathbb{R}^3 \rightarrow \mathbb{R}^3) \rightarrow H$ ) from the neighborhood of the parent node and its neighbors (where output probabilities  $\mathcal{H}(\mathcal{P}(n), l)$  were already computed in a previous step).

$$\begin{aligned} \text{smp}(n, t)[p] &= \text{nh}(n)[t(p)] \\ \text{brd}(h) &= \{(p, h[p]) \mid \{p_x, p_y, p_z\} \cap \{0, s_e - 1\} \neq \emptyset\} \\ \text{cl}(n, l) &= \begin{cases} \{\} & \mathcal{P}(n) = \epsilon \\ \text{brd}(\text{smp}(\mathcal{H}(\mathcal{P}(n), l), l), & \text{else} \\ \mathcal{T}_{\mathcal{P}(n)} \circ \mathcal{T}_n^{-1}) & \end{cases} \end{aligned}$$

User-defined labels are rasterized into the expanded brick and can thus directly influence the foreground probability map of the original brick. The probability map for the original brick is the  $s^3$ -sized center of the expanded result. Equation 1 can thus be completed to apply to all nodes:

$$\text{br}(\mathcal{H}(n, l, \beta)) = \text{ctr}(\text{rw}(\text{nh}(n), \mathcal{T}_n(l) \cup \text{cl}(n, l), \beta)) \quad (2)$$

A large factor  $e$  is advantageous due to the increased high resolution global context, but also results in an increase of computational time by a factor of  $\mathcal{O}(e^3)$ . We suggest  $e = 1.25$  as a balance between accuracy and run time.



### C. Adaptive Parameter Setting

A challenge (but also advantage) of the octree data structure is that noise on the full resolution level is reduced by the mean filtering in the construction of coarser levels. While reduced noise on coarser octree levels is obviously advantageous for application of the random walker method, it also implies that the optimal choice for  $\beta$  is dependent on the octree level. Hence, an automatic way of computing suitable parameters is required. This has the additional advantage that  $\beta$  can be adapted to regions with different noise levels within the image as well. Bian et al. [5] assume additive Gaussian noise and first estimate the global variance  $\sigma^2$  based on the intensity difference between the original image and estimated true intensities (obtained using a median filter  $f$ ). Then  $\beta$  is defined to normalize the (estimated true) intensity difference of two neighboring voxels by the estimated variance of intensity differences  $\sigma_d^2: H \rightarrow \mathbb{R}$  (which uses  $\sigma^2$  and  $f$ ):  $\beta_n = (2\sigma_d^2(nbh(n)))^{-1}$ . Equation 2 is thus further refined to use a  $\beta_n$  dependent on the current node:

$$\text{br}(\mathcal{H}(n, l)) = \text{ctr}(\text{rw}(\text{nh}(n), \mathcal{T}_n(l) \cup \text{cl}(n, l), \beta_n)) \quad (3)$$

Additionally, as  $\beta_n$  normalizes the estimated true voxel intensities, the edge weight function is modified to operate on  $f(b)$ :  $w_{p,q} = \exp(-\beta_n(f(b)[p] - f(b)[q])^2)$ .

The above method can be generalized to other noise models [12]. For datasets with Poisson noise (for example those in our real world data evaluation), the following edge function is used:  $w_{p,q} = \exp(-\frac{1}{2}(\sqrt{b[p]} - \sqrt{b[q]})^2)$ .

### D. Run Time Enhancements

While the preliminary framework description above (Equation 3) ensures accuracy and constant memory complexity, this section discusses run time enhancements that directly follow (iterative solver initialization, parallelization) or are enabled by the algorithm structure (pruning).

1) *Pruning*: When labeling objects larger than at least one brick (which is also the case when only labeling relatively few, small foreground objects, leaving large background regions) it is often unnecessary to complete the proposed procedure down to the leaf level for all branches of the tree. When the resulting foreground probability  $B$  of a node is *homogeneous* ( $\text{hom}: B \rightarrow \text{Bool}$ ), i.e., its range is smaller than a threshold  $t_{\text{hom}}$ , its children do not have to be processed.

$$\text{hom}(b) = (\max_{p \in [0, s]^3} b[p] - \min_{p \in [0, s]^3} b[p]) < t_m$$

In our experiments the threshold was set to  $t_{\text{hom}} = 0.3$ . Furthermore, if the user is not interested in the foreground probability volume itself, but in a binary segmentation (by thresholding the probability at  $p = 0.5$ ), nodes do not have to be processed further if the foreground/background state is already determined ( $\text{dt}: B \rightarrow \text{Bool}$ ). This is the case if the lowest foreground probability is above 0.5 (resulting in a brick) or the maximum is below 0.5 (resulting in a foreground brick) by a specific margin  $t_{\text{bin}}$ .

$$\text{dt}(b) = \min_{p \in [0, s]^3} b[p] - 0.5 > t_{\text{bin}} \vee 0.5 - \max_{p \in [0, s]^3} b[p] > t_{\text{bin}}$$

For a binary segmentation (i.e., the output probability map thresholded at 0.5) a low value of  $t_{\text{bin}} = 0.01$  is sufficient.

This pruning process may cause sampling probabilities for continuous labels at the border of the current brick to fail for neighbors of the parent node since the tree is no longer complete. In this case sampling continues at the nearest transitive parent of the absent node, in the worst case at the root node. Additionally, during the rasterization foreground and background labels may be in conflict ( $\text{cfl}: N \times L \rightarrow \text{Bool}$ ), i.e., occupy the same voxel:

$$\begin{aligned} \text{cfl}(n, l) &= \exists (q_0, p_0), (q_1, p_1) \in l : \\ &\quad [\mathcal{T}_n(q_0)] = [\mathcal{T}_n(q_1)] \wedge p_0 \neq p_1 \end{aligned}$$

In this case the voxel is left unlabeled and its output probability is determined by other non-conflicting labels. While this is normally not a problem on the leaf level (i.e., original resolution of the volume) for sensible user-defined labels, non-conflicting labels on the finest level can be in conflict when rasterized on a coarser octree level with a lower brick resolution. In the core procedure this is not problematic since the ambiguity is automatically resolved at a finer level. For pruning this means that children of nodes with label conflicts cannot be pruned and thus have to be processed even if they appear to be homogeneous or determined.

With the above definitions we can define  $\mathcal{H}_p$  as an optimized version of  $\mathcal{H}$  (from Equation 3):

$$\begin{aligned} \text{pruneable}(b) &= \text{hom}(b) \vee \text{dt}(b) \\ \mathcal{H}_p(n, l) &= \begin{cases} \epsilon & \text{pruneable}(\mathcal{H}(n, l)) \wedge \neg \text{cfl}(n, l) \\ \mathcal{H}(n, l) & \text{else} \end{cases} \end{aligned}$$

2) *Iterative Solver Initialization*: As noted by Grady [18], the system of linear equations is often efficiently solved using an iterative method [20], which can typically be accelerated by providing an initial state that is close to the true solution. For all but the root level this is the case in our method: As pointed out above, the foreground probability map computed for the parent brick of any node can be sampled to provide an approximation of the solution for the current level. This approximation is thus also used as an initialization for the iterative solver.

3) *Parallelization*: As all bricks within an octree layer are independent from one another, the computation can trivially be parallelized. While costly brick processing steps (such as filtering, edge weight computation and solving of linear equation systems) are parallelizable themselves, this makes the procedure well suited for parallelization on multiple GPUs in workstations.

### E. Incremental Labeling

The set of user-defined seeds in semi-automatic segmentation algorithms is typically not created in a single step, but built up incrementally in an evaluate-edit-compute cycle, in which the user inspects the existing segmentation, changes the parameters (seeds) of the algorithm and then waits for the algorithm to update the segmentation before starting the cycle again, inspecting the updated segmentation [31]. As such, computation time is not the only factor affecting the

total time to produce the desired segmentation result, but still very important, since high latency between user interaction and display of intermediate results impacts user performance [19]. Consequently, the *incremental run time* of an algorithm, in which the previous result is an additional input, has to be considered and evaluated.

Grady [18] suggests using the previous result as initialization for iterative solver for the standard random walker method. This is applicable here (even for non-iterative application, as described above), but not sufficient if the previous result octree is nearly complete: In this case operations such as loading (possibly from disk) and edge weight computations still have to be executed for all branches of the tree. Instead, we reuse entire branches of the previous result if they can be expected to be similar to the new result: After computing a new foreground probability map for a node if the result is sufficiently similar to the previous probability map of the corresponding node in the old tree, the new node is discarded and replaced by the old node *including* its children. With  $\mathcal{H}_{it}(n, l')$  as the previous solution for label set  $l'$ :

$$\mathcal{H}_{it}(n, l) = \begin{cases} \mathcal{H}_{it}(n, l') & \text{br}(\mathcal{H}_{it}(n, l')) \approx \text{br}(\mathcal{H}(n, l)) \\ & \wedge \neg \text{cfl}(n, l) \\ \mathcal{H}(n, l) & \text{else} \end{cases}$$

Similar to pruning, if there are conflicts in the set of (changed) labels affecting this brick, this optimization cannot be performed, but it is sufficient to consider conflicts where at least one of the recently added labels ( $l - l'$ ) is involved. Pruning and incremental labeling can of course be combined. Probability maps are considered similar if the maximum pairwise difference is below a threshold  $t_{inc}$ . We set  $t_{inc} = 0.01$  in all experiments.

$$b_0 \approx b_1 \Leftrightarrow \max_{p \in [0, s]^3} (|b_0[p] - b_1[p]|) < t_{inc}$$

## V. EVALUATION AND DISCUSSION

In this section the proposed framework is applied to synthetic and real world datasets of up to 377 GB in size and the results are discussed. Where possible accuracy and run time are compared to the basic method. All experiments were carried out on a standard PC with an Intel i5-6500 (3.2 GHz, 4 core), 16 GB RAM, a single NVidia GTX 1060 (6 GB RAM) and a Samsung EVO 970 SSD.

### A. Synthetic Data

For comparison with the basic approach, we generate a ground-truth volume (binary segmentation), a noisy input volume (with a mean of 0.3/0.7 for background/foreground and additive Gaussian noise with varying  $\sigma$ ), as well as foreground and background labels defined as points or lines. Foreground structures cover 1% of the total volume. The *structure size* range is a parameter that influences the size of individual foreground objects and is relative to the dataset size. The upper bound (*structure size* in the following) is 10% if not specified otherwise. The lower bound is always half of the *structure size*. Existing frameworks for biomedical test data generation [22] are limited in the size of datasets which can be generated.

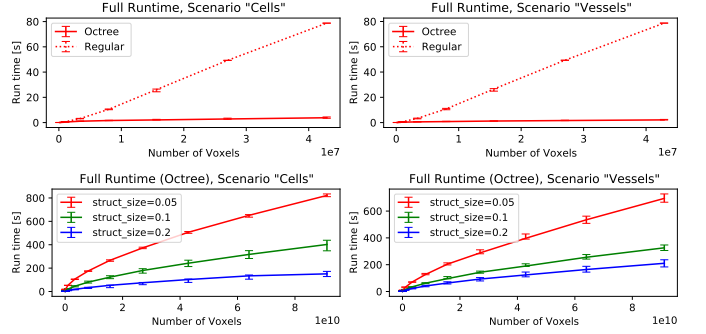


Fig. 3. Median wall-clock run time of the regular random walker and proposed octree variant (top row), and octree variant for larger volume sizes and varying structure sizes (bottom row). Error bars show minimum/maximum run times.

Therefore we define structures as described below and create a voxel representation by organizing the primitives (spheres, cylinders) in sorted queues (according to their bounding boxes) for the  $z$ ,  $y$  and  $x$ -dimension, scanning the output volume linearly, for each voxel rasterizing active primitives [13]. We chose the following biomedical application-inspired scenarios:

*Cells* are represented as spheres with a radius within structure size and placed randomly within the volume. Centers of spheres do not intersect other spheres, allowing for “clustering” of cells. Foreground seeds are placed at the center of each sphere. For each generated sphere background seeds are generated between two randomly selected spheres and between a sphere and the nearest volume border in each of the coordinate axes (if the space is available).

*Vessels* consist of segments of cylindrical shape and spheres at branching points. Each vessel tree starts with a radius within the structure size from a random point at the volume border. The vessel branches at  $5 \times$  radius into two segments, preserving cross-section area. This process repeats recursively. The vessel centerline is added to the set of foreground labels and a number (roughly equal to the voxel length of the segment) of point background labels are placed at random radial positions. Additionally, similar to the *Cells* scenario, background seeds are positioned between branching points and the nearest volume borders.

All experiments have been executed 5 times with different seeds for the random number generator so that minimum, median and maximum performance can be evaluated.

1) *Full Run Time*: Figure 3 (top row) compares the run time of the basic random walker [18] to the proposed octree variant (using the regular variant [18] as a component) on synthetic datasets up to a volume size of  $350 \times 350 \times 350$ . Larger volumes could not be processed by the regular variant due to limited graphics memory. The bottom row hence only shows the octree variant, up to a volume size of  $4500 \times 4500 \times 4500$  voxels (182 GB). In direct comparison, the octree variant is considerably faster than the regular random walker. This becomes even more apparent for increasing dataset sizes. For  $350^3$  voxel datasets the original variant requires more than a minute of computation time (independent of the scenario) while the proposed method completes in less than 4s. Furthermore, while the run time of the regular approach is shown to be linear, the run time of the proposed framework

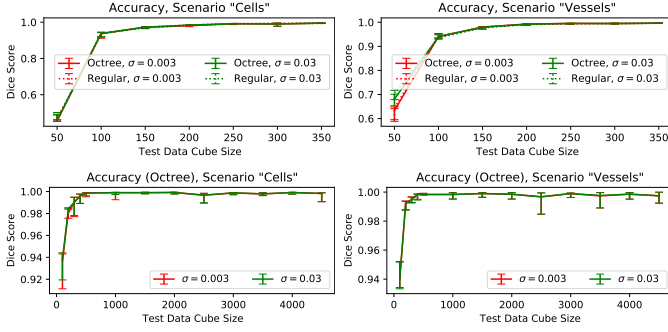


Fig. 4. Median Dice score of the generated segmentation compared to ground truth for regular random walker and octree variant (top row), and the octree variant for larger volume sizes (bottom row). Error bars show minimum/maximum scores.

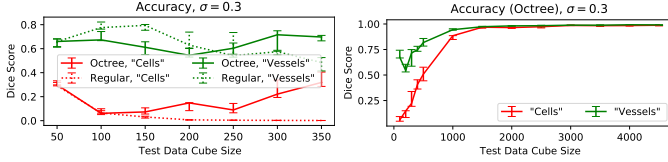


Fig. 5. Median Dice score of the generated segmentation compared to ground truth for high noise levels ( $\sigma = 0.3$ ). Error bars show minimum/maximum scores.

appears sub-linear. Indeed, due to pruning, at any level only bricks intersecting a foreground-background boundary within the volume require further processing (in assumed perfect conditions). As the (relative) structure size of the test datasets is constant for different volume sizes, at each octree level, the 2D surfaces of objects only intersect with  $\mathcal{O}(n^{\frac{2}{3}})$  of  $n$  bricks<sup>2</sup>, resulting in an asymptotic run time of  $\mathcal{O}(n^{\frac{2}{3}})$ . This is supported by the fact that smaller structure sizes (resulting in a *higher number* of structures and ultimately more surface area) cause longer computation times.

To evaluate the accuracy of the regular and hierarchical variant, the generated segmentation (using a threshold of 0.5 on the foreground probability map) was compared to the ground truth segmentation using the Dice index. The results are depicted in Figure 4. For low and medium noise levels ( $\sigma = 0.003$  and  $\sigma = 0.03$ ) regular and octree variant yield similar results. Here, the Dice score increases for larger volume sizes and is above 0.9 for sizes larger than 50. Both the increase and low score for a volume size of 50 can be explained by the median filter applied during the adaptive parameter setting which disturbs the border of objects. This effect is reduced when the resolution (i.e., volume size) increases. For datasets larger than  $500^3$  voxels, the minimum Dice score of the octree variant does not drop below 0.98 and in the median stays above 0.995.

Figure 5 shows that for strong noise  $\sigma = 0.3$  (i.e., almost as large as the difference between mean foreground (0.7) and background (0.3) values), both variants struggle to produce the expected result for small volume sizes. This is especially true for the cell scenario, possibly due to fewer seeds points from

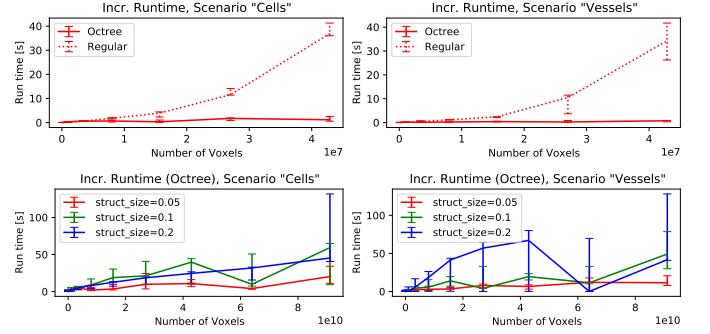


Fig. 6. Median wall-clock run time after adding a label for a previously unlabeled foreground component for regular random walker and octree variant (top row), and for the octree variant with larger volume sizes and varying structure sizes (bottom row). Error bars show minimum/maximum run times.

the dataset generation. However, while the regular random walker variant produces increasingly bad scores for larger volumes, the octree variant starts to improve at a volume size of roughly 200 or 250. For volumes larger than  $1500^3$  voxels Dice scores consistently above 0.95 are achieved. The mean filtering of the LOD approach can be expected to reduce the (additive) noise at the coarser levels of the pyramid, allowing the broad structure of foreground objects to be captured, even when the exact surface features cannot be reconstructed due to the noise.

2) *Simulation of Incremental Labeling:* In order to demonstrate run time savings of the incremental labeling aspect of the proposed approach, two subsequent runs are performed to simulate a single user editing step. In the first run, a randomly selected foreground label (a single centerpoint of a sphere or the centerline of a vessel segment) is retained from the complete set of labels. For the second run this label is added and the run time is measured.

Figure 6 shows the incremental run time for the regular and octree random walker approach in comparison, and for the octree variant for datasets larger than  $350^3$  voxels. Both appear to benefit from the additional information of a previous solution. However, for the regular random walker, a super-linear median run time can be observed and for the largest dataset ( $350^3$  voxels) roughly 25-40 seconds processing time are required for both scenarios. The proposed octree variant shows moderate increase in computation time from less than 1 second for the smallest dataset ( $50^3$  voxels) to a median of 1-2 seconds for the largest dataset shown in this graph, which is a further reduction in comparison with the full (non-incremental run time) shown in Figure 3.

In contrast to the full run time evaluation, structure sizes have a different effect: The overall trend is that larger structure sizes require more computation time. This is expected, as (in contrast to the full computation) only a single structure element requires modification. Smaller structures thus require less work overall. For a structure size of 0.05, a median time of up to 10 seconds is required. Minimum and maximum do not deviate by more than 15 seconds. Larger structures (structure size 0.2, spanning large portion of volume), result in higher processing times up to roughly 40 seconds (median). This is significantly lower than for the full computation and

<sup>2</sup>Sketch of proof: If the volume of the (non-fractal) structure  $V(\alpha) \in \mathcal{O}(\alpha^3)$  grows cubically with the scale  $\alpha$  of the structure, its surface intersects with less than  $\frac{V(d+\alpha)-V(d-\alpha)}{\alpha^3} \in \mathcal{O}(\alpha^2)$  bricks for a constant  $c$ .



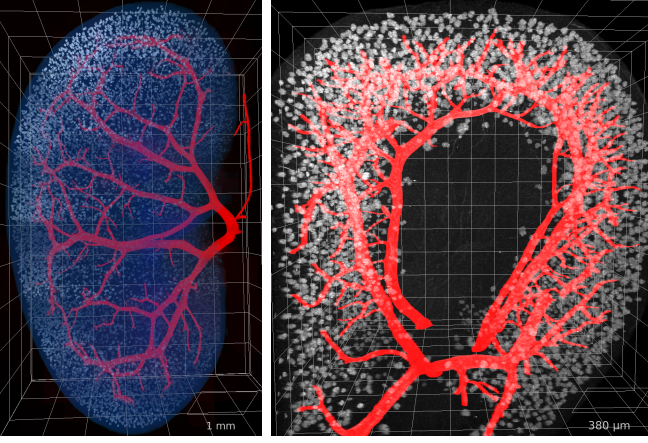


Fig. 7. Raycasting rendering of the kidney dataset (377 GB left, 60 GB right) mainly showing high intensity glomeruli (grayscale), including the arterial vessel tree (red) and kidney volume (blue) segmentation obtained using the proposed method. The resulting vessel networks have a total length of 164 mm (left) and 170 mm (right) and a volume of  $0.67 \text{ mm}^3$  (left) and  $0.35 \text{ mm}^3$  (right).

still usable in practice considering that volumes with large structures likely require few labels overall. The accuracy of both the regular and octree approach were observed to be equivalent to non-incremental runs.

### B. Real Data

We evaluate the proposed approach on data that is used in current biomedical research [25], an antibody-stained light sheet microscopy scan of a mouse kidney. There, the proposed method is applied to semi-automatically generate foreground segmentations as part of the analysis pipeline. As ground truth data is not available, a quantitative accuracy analysis was not possible, but the created segmentations were perceived to be of high quality by biomedical experts and used for further analysis of the vessel network [25]. In total three labeling tasks were carried out: 1) A binary segmentation of the arterial vasculature (up to the capillary level) created on a 60 GB subset of the whole dataset; 2) The vascular tree of the 377 GB dataset up to a vessel radius of about  $50 \mu\text{m}$  was created in the same way; 3) A foreground mask for the whole kidney volume was created in a similar fashion. Figure 7 shows a rendering of the dataset, the vasculature and whole kidney segmentation for illustration and a smaller dataset with a more detailed segmentation of the vasculature.

Table I shows some additional information about the datasets, including the full computation time (without a previous result, given the full set of labels) and observed computation time ranges for updates to the label set. The observed full computation time is in line with the results of the synthetic dataset experiments (see Figure 3) and thus substantial, but satisfactory in practice (below one hour) given the size of the datasets. For vasculature the incremental computation times are observed to be in the order of seconds (especially for smaller vessels (1s), but also for the long sections of the largest vessels (60s)) and are thus dominated or roughly equivalent to the time a user needs for inspection and interaction with

the data. For the full kidney segmentation individual changes to the label set require a longer run time to update the output probability map (between few minutes and the full run time). This, however, is balanced out by the fact that very few labels in general are required. In general, regions of high uncertainty (i.e., foreground probability values around 0.5) cause longer computation times since those regions often cannot be pruned. This was also the case for the kidney, where three foreground labels in the center and two on the outside were able to cleanly separate foreground from background at the capsule, but failed to define a clear boundary at the hilum where vessels are entering the kidney. Here, a number of additional labels were required to remove the ambiguity. Thus, a sudden increase of computation time signifies resulting uncertainty in the segmentation and may prompt to correct the last set of labels and restart the computation.

The total label time (including user interaction) was roughly three hours for the large vasculature in the full 377GB dataset, and about seven hours for the 60GB subset with substantially more detail. The broad majority of this time can be attributed to the user interaction and identification of vessels itself, since the segmented vessels are often of comparatively low intensity, which also makes the application of fully automated method difficult. The Kidney segmentation is dominated by the whole compute time since the initial set of labels already generated a good segmentation of the whole kidney and few corrections were required. The user interaction time itself was in the order of minutes.

## VI. CONCLUSION

We have presented a scalable approximation of the random walker method for semi-automatic segmentation of very large volumetric datasets. It can be applied to volumes that exceed the main and graphics memory capacity and outperforms the original variant in run time performance while preserving accuracy on the examined test datasets. The approach can process large datasets on consumer PCs, but at the same time is future-proof and scalable beyond the experiments in this paper, as it is easily parallelizable and should be able to fully utilize multi-GPU setups. The presented method is meanwhile part of version 5.2 of Voreen, a widely used open source volume rendering and processing framework.

In the future, we like to further improve the current implementation by moving more computations, such as pre-processing (median filter, adaptive parameters) and linear equation system construction, from the CPU onto the GPU, thus further improving the scalability. We will explore the integration of extensions to random walker algorithm [37] (such as automatic label generation [1]). Furthermore, it is worth investigating the use of other compatible methods that compute segmentation probability maps from user-defined seeds in our framework that is of general nature.

## REFERENCES

- [1] Shawn Andrews, Ghassan Hamarneh, and Ahmed Saad. Fast random walker with priors using precomputation for interactive medical image segmentation. In Tianzi Jiang, Nassir Navab, Josien P. W. Pluim, and Max A. Viergever, editors, *Proc. of Medical Image Computing and*

TABLE I

INFORMATION ABOUT THE PROCESSED REAL WORLD DATASETS INCLUDING FULL RUN TIME (WITHOUT PREVIOUS RESULTS AND WITH THE FULL LABEL SET) AND TIME RANGES FOR LABEL UPDATE OPERATIONS.

| Dataset              | Voxel Dimensions                | Real Dimensions                          | Size   | Full Run Time | Incr. Run Time |
|----------------------|---------------------------------|--|--------|---------------|----------------|
| Vasculature (Subset) | $5153 \times 4791 \times 1213$  | $3.9 \times 3.6 \times 3.6 \text{ mm}^3$ | 60 GB  | 10 min        | 1 s–15 s       |
| Vasculature (Full)   | $9070 \times 12732 \times 1634$ | $6.8 \times 9.6 \times 4.9 \text{ mm}^3$ | 377 GB | 11 min        | 1 s–60 s       |
| Full Kidney (Full)   | $9070 \times 12732 \times 1634$ | $6.8 \times 9.6 \times 4.9 \text{ mm}^3$ | 377 GB | 48 min        | 4 min–48 min   |

- Computer-Assisted Intervention (MICCAI), Part III*, volume 6363 of *LNCS*, pages 9–16. Springer, 2010. 1, 7
- [2] Ulas Bagci, Jayaram K. Udupa, Neil Mendhiratta, Brent Foster, Ziyue Xu, Jianhua Yao, Xinjian Chen, and Daniel J. Mollura. Joint segmentation of anatomical and functional images: Applications in quantification of lesions from PET, PET-CT, MRI-PET, and MRI-PET-CT images. *Medical Image Anal.*, 17(8):929–945, 2013. 1
- [3] Ulas Bagci, Jayaram K. Udupa, Jianhua Yao, and Daniel J. Mollura. Co-segmentation of functional and anatomical images. In Nicholas Ayache, Hervé Delingette, Polina Golland, and Kensaku Mori, editors, *Proc. of Medical Image Computing and Computer-Assisted Intervention (MICCAI), Part III*, volume 7512 of *LNCS*, pages 459–467. Springer, 2012. 1
- [4] Katie Bentley, Claudio Areias Franco, Andrew Philippides, Raquel Blanco, Martina Dierkes, Véronique Gebala, Fabio Stanchi, Martin Jones, Irene M Aspalter, Guiseppe Cagna, et al. The role of differential VE-cadherin dynamics in cell rearrangement during angiogenesis. *Nature Cell Biology*, 16(4):309, 2014. 1
- [5] Ang Bian and Xiaoyi Jiang. Statistical modeling based adaptive parameter setting for random walk segmentation. In Jacques Blanc-Talon, Cosimo Distanto, Wilfried Philips, Dan Popescu, and Paul Scheunders, editors, *Advanced Concepts for Intelligent Vision Systems*, pages 698–710. Springer, 2016. 1, 4
- [6] Pablo Blinder, Philbert S Tsai, John P Kaufhold, Per M Knutsen, Harry Suhl, and David Kleinfeld. The cortical angiome: an interconnected vascular network with noncolumnar patterns of blood flow. *Nature Neuroscience*, 16(7):889, 2013. 1
- [7] Yuri Boykov and Marie-Pierre Jolly. Interactive graph cuts for optimal boundary and region segmentation of objects in N-D images. In *Proc. of the Eighth International Conference on Computer Vision (ICCV), Volume I*, pages 105–112. IEEE Computer Society, 2001. 1
- [8] Tobias Brix, Jörg-Stefan Praßni, and Klaus Hinrichs. Visualization of large volumetric multi-channel microscopy data streams on standard PCs. In *BioVis: 4th Symposium on Biological Data Visualization*, 2014. 2
- [9] Lorenzo Cerrone, Alexander Zeilmann, and Fred A. Hamprecht. End-to-end learned random walker for seeded image segmentation. In *IEEE Conference on Computer Vision and Pattern Recognition (CVPR)*, pages 12559–12568, 2019. 1
- [10] Yung-fu Chen, Po-Chi Huang, Ker-Cheng Lin, Hsuan-Hung Lin, Li-En Wang, Chung-Chuan Cheng, Tsung-Po Chen, Yung-Kuan Chan, and John Y. Chiang. Semi-automatic segmentation and classification of pap smear cells. *IEEE J. Biomed. Health Informatics*, 18(1):94–108, 2014. 1
- [11] Cyril Crassin, Fabrice Neyret, Sylvain Lefebvre, and Elmar Eisemann. Gigavoxels: ray-guided streaming for efficient and detailed voxel rendering. In Eric Haines, Morgan McGuire, Daniel G. Aliaga, Manuel M. Oliveira, and Stephen N. Spencer, editors, *Proc. of Symposium on Interactive 3D Graphics (SI3D)*, pages 15–22. ACM, 2009. 2
- [12] Dominik Drees and Xiaoyi Jiang. Bayesian reasoning based adaptive parameter setting for random walk segmentation under arbitrary noise models. *in preparation*. 4
- [13] Dominik Drees and Xiaoyi Jiang. Efficiently sampling large images from bounded functions. *in preparation*. 5
- [14] Dominik Drees, Aaron Scherzinger, René Hägerling, Friedemann Kiefer, and Xiaoyi Jiang. Scalable robust graph and feature extraction for arbitrary vessel networks in large volumetric datasets. *CoRR*, abs/2102.03444, 2021. 1
- [15] Anna Fabijanska and Jaroslaw Goclawski. The segmentation of 3d images using the random walking technique on a randomly created image adjacency graph. *IEEE Trans. Image Process.*, 24(2):524–537, 2015. 2
- [16] Ling Ge, Ran Ju, Tongwei Ren, and Gangshan Wu. Interactive RGB-D image segmentation using hierarchical graph cut and geodesic distance. In *Pacific Rim Conference on Multimedia*, pages 114–124. Springer, 2015. 1
- [17] Cynthia Gerlein-Safdi and Christopher S Ruf. A CYGNSS-based algorithm for the detection of inland waterbodies. *Geophysical Research Letters*, 46(21):12065–12072, 2019. 1
- [18] Leo Grady. Random walks for image segmentation. *IEEE Trans. Pattern Anal. Mach. Intell.*, 28(11):1768–1783, 2006. 1, 2, 3, 4, 5
- [19] Houssein-Eddine Gueziri, Michael J. McGuffin, and Catherine Laporte. Latency management in scribble-based interactive segmentation of medical images. *IEEE Trans. Biomed. Eng.*, 65(5):1140–1150, 2018. 5
- [20] Wolfgang Hackbusch. *Iterative Solution of Large Sparse Systems of Equations*, volume 95 of *Applied Mathematical Sciences*. Springer, 1994. 2, 4
- [21] René Hägerling, Cathrin Pollmann, Martin Andreas, Christian Schmidt, Harri Nurmi, Ralf H Adams, Kari Alitalo, Volker Andresen, Stefan Schulte-Merker, and Friedemann Kiefer. A novel multistep mechanism for initial lymphangiogenesis in mouse embryos based on ultramicroscopy. *The EMBO Journal*, 32(5):629–644, 2013. 1
- [22] Ghassan Hamarneh and Preet Jassi. Vascusynth: Simulating vascular trees for generating volumetric image data with ground truth segmentation and tree analysis. *Computerized Med. Imaging and Graphics*, 34(8):605–616, 2010. 5
- [23] Nicholas Hamilton. Quantification and its applications in fluorescent microscopy imaging. *Traffic*, 10(8):951–961, 2009. 1
- [24] Chaoren Hu, Hui Hui, Shuo Wang, Di Dong, Xia Liu, Xin Yang, and Jie Tian. Cerebral vessels segmentation for light-sheet microscopy image using convolutional neural networks. In *Medical Imaging: Biomedical Applications in Molecular, Structural, and Functional Imaging*, page 101370K, 2017. 2
- [25] Nils Kirschnick, Dominik Drees, Esther Redder, Raghu Erapanneedi, Abel Pereira da Graca, Michael Schäfers, Xiaoyi Jiang, and Friedemann Kiefer. Rapid methods for the evaluation of fluorescent reporters in tissue clearing and the segmentation of large vascular structures. *under review*. 7
- [26] C. Kirst, Sophie Skriabine, Alba Vieites-Prado, and N. Renier. Mapping the fine-scale organization and plasticity of the brain vasculature. *Cell*, 180:780–795, 2020. 1
- [27] Eric LaMar, Mark A. Duchaineau, Bernd Hamann, and Kenneth I. Joy. Multiresolution techniques for interactive texture-based rendering of arbitrarily oriented cutting planes. In Wim C. de Leeuw and Robert van Liere, editors, *Proc. of Joint Eurographics and IEEE TCVG Symposium on Visualization, VisSym*, pages 105–114. Eurographics Association, 2000. 2
- [28] Jiahui Li, Shuang Yang, Xiaodi Huang, Qian Da, Xiaoqun Yang, Zhiqiang Hu, Qi Duan, Chaofu Wang, and Hongsheng Li. Signet ring cell detection with a semi-supervised learning framework. In Albert C. S. Chung, James C. Gee, Paul A. Yushkevich, and Siqi Bao, editors, *Proc. of Information Processing in Medical Imaging - 26th International Conference (IPMI)*, volume 11492 of *LNCS*, pages 842–854. Springer, 2019. 1
- [29] Geert Litjens, Thijs Kooi, Babak Ehteshami Bejnordi, Arnaud Arindra Adiyoso Setio, Francesco Ciompi, Mohsen Ghafoorian, Jeroen A. W. M. van der Laak, Bram van Ginneken, and Clara I. Sánchez. A survey on deep learning in medical image analysis. *Medical Image Anal.*, 42:60–88, 2017. 2
- [30] S Mathewlynn and SL Collins. Volume and vascularity: Using ultrasound to unlock the secrets of the first trimester placenta. *Placenta*, 84:32–36, 2019. 1
- [31] Silvia Delgado Olabarriaga and Arnold W. M. Smeulders. Interaction in the segmentation of medical images: A survey. *Medical Image Anal.*, 5(2):127–142, 2001. 4
- [32] J. Prassni, R. Ropinski, and K. Hinrichs. Uncertainty-aware guided volume segmentation. *IEEE Transactions on Visualization and Computer Graphics*, 16(6):1358–1365, 2010. 1
- [33] Jianbing Shen, Yunfan Du, Wenguan Wang, and Xuelong Li. Lazy random walks for superpixel segmentation. *IEEE Trans. Image Process.*, 23(4):1451–1462, 2014. 1
- [34] Zhenghao Shi, Jiejue Ma, Minghua Zhao, Yonghong Liu, Yaning Feng, Ming Zhang, Lifeng He, and Kenji Suzuki. Many is better than one: an integration of multiple simple strategies for accurate lung segmentation



- in CT images. *BioMed Research International*, 2016, 2016. [1](#)
- [35] Manibarathi Vaithiyanathan, Nora Safa, and Adam T Melvin. Fluorocell-track: An algorithm for automated analysis of high-throughput droplet microfluidic data. *PLoS ONE*, 14(5):e0215337, 2019. [1](#)
- [36] Feng Wang, Ingo Wald, and Chris R. Johnson. Interactive rendering of large-scale volumes on multi-core cpus. In *9th IEEE Symposium on Large Data Analysis and Visualization (LDAV)*, pages 27–36. IEEE, 2019. [2](#)
- [37] Zhaobin Wang, Lijie Guo, Shuai Wang, Lina Chen, and Hao Wang. Review of random walk in image processing. *Archives of Computational Methods in Engineering*, 26:17–34, 2019. [1](#), [3](#), [7](#)
- [38] Manfred Weiler, Rüdiger Westermann, Charles D. Hansen, Kurt Zimmerman, and Thomas Ertl. Level-of-detail volume rendering via 3D textures. In William E. Lorensen, Roger Crawfis, and Daniel Cohen-Or, editors, *Proc. of Visualization and Graphics Symposium, (VVS)*, pages 7–13. ACM / IEEE Computer Society, 2000. [2](#)
- [39] Yang Xiao and Jie Hu. Hierarchical random walker for multimodal brain tumor segmentation. *MICCAI Challenge on Multimodal Brain Tumor Segmentation*, 2012. [1](#)
- [40] Tianwen Xie, Zhe Wang, Qiufeng Zhao, Qianming Bai, Xiaoyan Zhou, Yajia Gu, Weijun Peng, and He Wang. Machine learning-based analysis of MR multiparametric radiomics for the subtype classification of breast cancer. *Frontiers in Oncology*, 9:505, 2019. [1](#)
- [41] Tianwen Xie, Qiufeng Zhao, Caixia Fu, Qianming Bai, Xiaoyan Zhou, Lihua Li, Robert Grimm, Li Liu, Yajia Gu, and Weijun Peng. Differentiation of triple-negative breast cancer from other subtypes through whole-tumor histogram analysis on multiparametric MR imaging. *European Radiology*, 29(5):2535–2544, 2019. [1](#)
- [42] Ziyue Xu, Ulas Bagci, Brent Foster, Awais Mansoor, and Daniel J. Mollura. Spatially constrained random walk approach for accurate estimation of airway wall surfaces. In Kensaku Mori, Ichiro Sakuma, Yoshinobu Sato, Christian Barillot, and Nassir Navab, editors, *Proc. of Medical Image Computing and Computer-Assisted Intervention (MICCAI), Part II*, volume 8150 of *LNCS*, pages 559–566. Springer, 2013. [1](#)
- [43] Wenxian Yang, Jianfei Cai, Jianmin Zheng, and Jiebo Luo. User-friendly interactive image segmentation through unified combinatorial user inputs. *IEEE Trans. Image Process.*, 19(9):2470–2479, 2010. [1](#)
- [44] Shan Zhao, M. Todorov, Ruiyao Cai, and Ali Ertürk. Cellular and molecular probing of intact human organs. *Cell*, 180:796–812, 2020. [1](#)